Chapter 4
Imaging the Human Body: Micro- and Nanostructure of Human Tissues

Georg Schulz, Hans Deyhle, and Bert Müller

Abstract Computed tomography based on X-rays is known to provide the best spatial resolution of all clinical three-dimensional imaging facilities and currently reaches a fraction of a millimeter. Better spatial and density resolution is obtained by means of micro computed tomography well established in the field of materials science. It is also very supportive imaging human tissues down to the level of individual cells (Lareida et al. J. Microsc. 234:95, 2009). The article demonstrates the power of micro computed tomography for imaging parts of the human body such as teeth, inner ear, cerebellum, tumors, and urethral tissue with conventional X-ray sources and synchrotron radiation facilities in absorption and phase contrast modes. The second part of the chapter relies on scanning X-ray scattering of tooth slices (Müller et al. Eur. J. Clin. Nanomed. 3:30, 2010) to uncover the presence of nanostructures including their anisotropy and orientation. This imaging technique gives unrivalled insights for medical experts, which will have a major influence on fields such as dental and incontinence treatments.

4.1 Introduction

Physicists fully understand the handling of hydrogen atoms and molecules. Molecules such as carbon dioxide, however, are already too big to be treated by physicists. Dealing with organic molecules already needs additional experts (chemists). Biomolecules such as proteins are even more complex and biological matter as an individual cell is already another subject.

Medical doctors have different approaches. They do handle the human body as a whole and take decisions within very short periods of time mainly on their

G. Schulz · H. Deyhle · B. Müller (✉)
Biomaterial Science Center, University Basel, c/o University Hospital Basel, 4031 Basel, Switzerland
e-mail: georg.schulz@unibas.ch; hans.deyhle@unibas.ch; bert.mueller@unibas.ch

S. Logothetidis (ed.), *Nanomedicine and Nanobiotechnology*, NanoScience and Technology, DOI 10.1007/978-3-642-24181-9_4,
© Springer-Verlag Berlin Heidelberg 2012

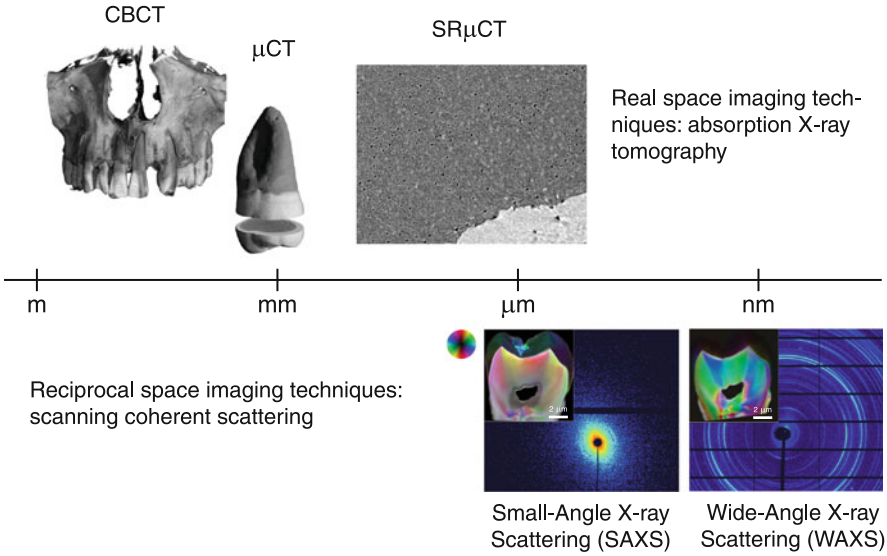

Fig. 4.1 X-ray imaging techniques and their corresponding length scale regimes

strong experience. Sometimes, however, they take benefit from radiology to get insight into the body. The three-dimensional imaging facilities of radiologists reach submillimeter resolution as indicated by the cone beam computed tomography cone beam tomography (CBCT) image in Fig. 4.1. Although these imaging facilities are extremely helpful in diagnosis and therapy and often yield a huge amount of data, their spatial resolution is far from the atomic scale.

This chapter is an attempt to bridge the gap between advanced radiology and the atomic world of solid-state physicists. The path is depicted in Fig. 4.1. Micro computed tomography (μCT) as well introduced in materials science allows mapping the microstructures within human tissues, if the contrast (density resolution) is reasonable. Using monochromatic X-ray beams, as usually done in synchrotron radiation-based μCT (SRμCT), improves the contrast of the three-dimensional data so that tiny microstructures such as the dentinal tubules (see Fig. 4.1) come to light. This, however, is the actual limit of hard X-ray tomography, if the application of X-ray optics is avoided. Nanostructures between 1 and 100 nm known from nanotechnology cannot be visualized.

X-ray diffraction using photon energies of about 10 keV, however, permits the characterization of these nanostructures as the average value obtained from the illuminated volume. The focusing of the X-ray beam to true micrometer diameters combined with scanning provides spatially resolved information on all kinds of nanostructures present. The related techniques are termed scanning small-angle X-ray scattering (SAXS) and scanning wide-angle X-ray scattering (WAXS), respectively (see Fig. 4.1). Spatially resolved SAXS and related images from human tissue will be discussed in detail below.

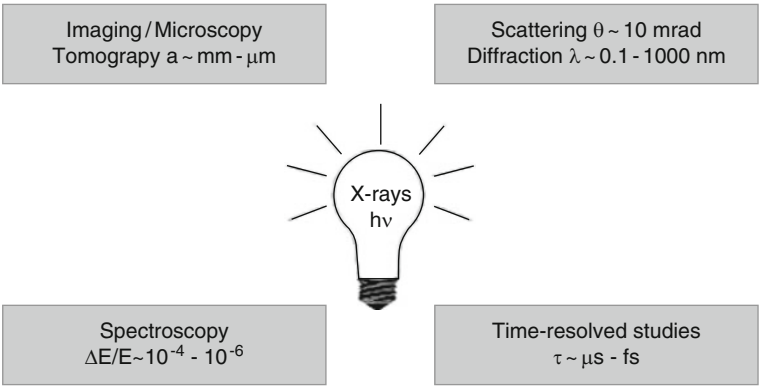

Fig. 4.2 Categories of methods to study human tissues with X-rays

The different X-ray-based techniques can be divided into four categories as shown in Fig. 4.2. Tomography (imaging) and scattering are often employed to characterize biological matter. For spectroscopy and time-resolved studies, only a very few examples are known and, therefore, these methods are not covered in this chapter. There are also methods, which belong to more than one of the categories and thus represent a combination [1].

4.2 Results and Discussion

4.2.1 X-Rays from Synchrotron Facilities

Synchrotron radiation sources provide such a high intensity that by using monochromators, one can easily build a tunable X-ray source. These developments allowed improving the imaging techniques in different manner. The main components of a synchrotron radiation facility, besides the storage ring, are the insertion device, the monochromator and the so-called endstation (Fig. 4.3). Electrons or positrons are injected into the synchrotron ring at high energies by either a linear accelerator or by an intermediate synchrotron which again is fed by a linear accelerator. Synchrotron radiation arises from magnetic deflection of the particle beam by the insertion device. The nowadays existing insertion devices are bending magnet, wiggler, undulator, and free-electron laser (Fig. 4.4). Whereas the X-rays induced by the first and second generation insertion devices interfere incoherently, a coherent interference appears for the third and fourth generation devices. Besides the different principles, the insertion devices vary in the intensity distribution and the brilliance of the generated X-rays. The main advantage of synchrotron light is its high intensity. This permits to select one photon energy from the polychromatic spectrum

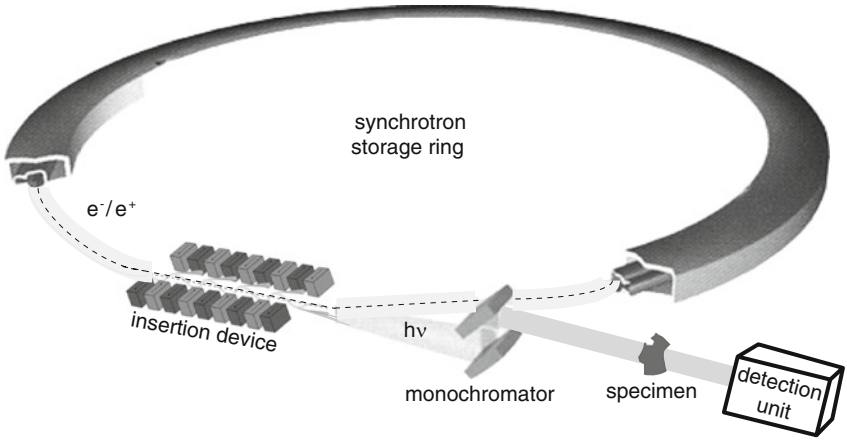

Fig. 4.3 Layout of a synchrotron radiation facility

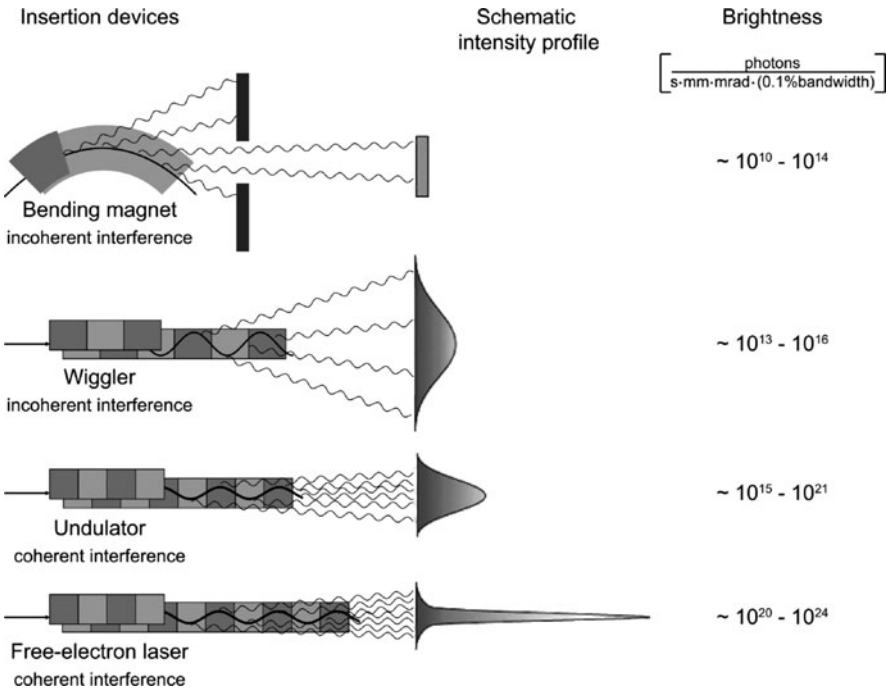

Fig. 4.4 Generation of X-rays with different insertion devices

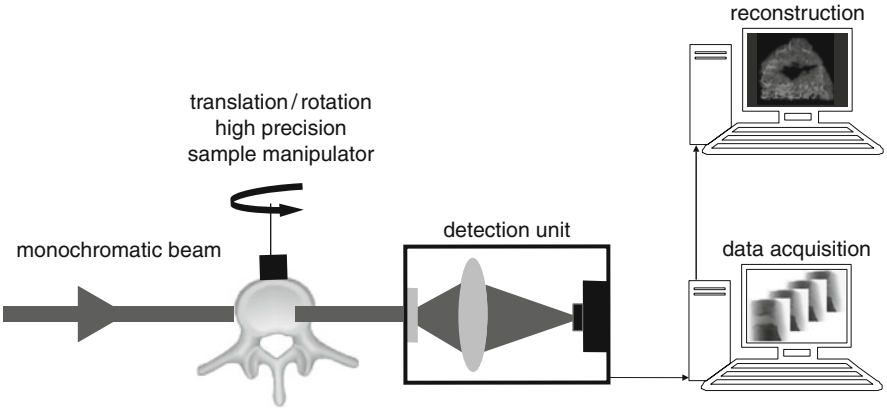

Fig. 4.5 Tomographic data acquisition and processing

generated in the insertion devices by means of a monochromator. X-ray energies used at synchrotron facilities range from several hundred eV to a few hundred keV.

4.2.2 Principles of Computed Tomography

The discovery of X-rays by Röntgen in 1895 [2] involved new applications in medicine both for diagnosis and therapy. Unfortunately, the information obtained by X-ray radiography does not include the whole three-dimensional information of the object. This three-dimensional information can be achieved by tomography. The principles of a tomographic data acquisition can be seen in Fig. 4.5. Using a high precision sample manipulator (translation and rotation), several hundreds of projections of the specimen can be acquired by the detection unit. The mathematical theory for the reconstruction of an object from the projections was proposed for the first time by Radon in 1917 [43]. Today, the three-dimensional information of the object results from creating sinograms from the projections and filtered backprojection reconstruction (Fig. 4.6) [3]. The additional advantage of tomography compared to transmission radiography, besides the three-dimensional information, is the much higher density resolution.

4.2.3 Absorption Contrast CT

For the investigation of human hard tissue, CT in absorption contrast mode is a widely used technique. The reconstructed dataset contains information about the three-dimensional distribution of the attenuation coefficient $\mu(x, y, z, E, Z, \rho)$ with the photon energy E, the atomic number Z, and the mass density of the specimen ρ.

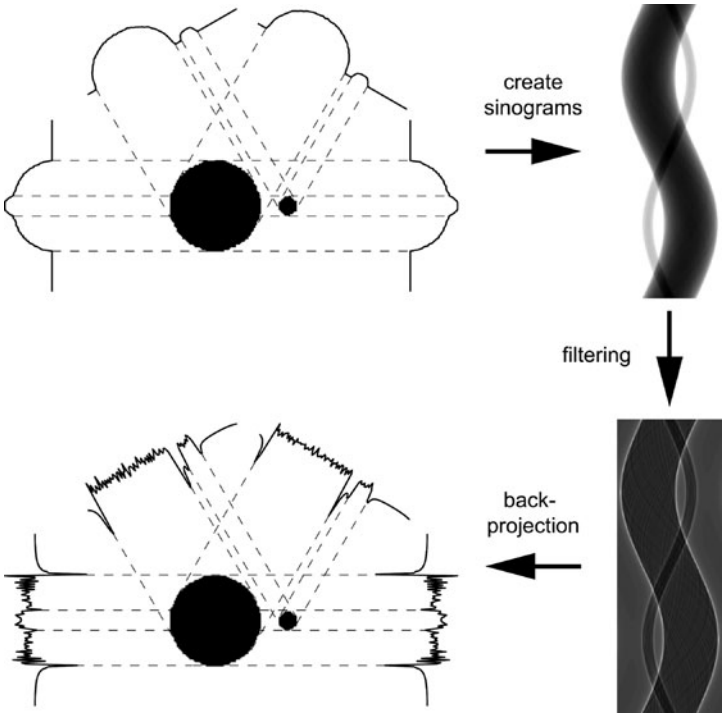

Fig. 4.6 Principle of tomographic data reconstruction by filtered backprojection algorithm

The approximate dependence between the attenuation coefficient and the photon energy of the incoming X-rays

$$\mu \sim \left(\frac{Z}{E}\right)^m \quad \text{with} \quad 2.5 < m < 3.5 \tag{4.1}$$

is valid in the region between two absorption edges [4]. The optimal energy for the scan can be estimated by the equation

$$\mu(Z, E) \cdot D = 2, \tag{4.2}$$

where D is the diameter of the specimen [5].

4.2.3.1 Visualization of Tumor Vessels

The formation of blood vessels in the human body, the so-called angiogenesis, is a crucial step for the initiation, survival, and metastases formation of malignant tumors. For the understanding of the biological regulation of it and in order

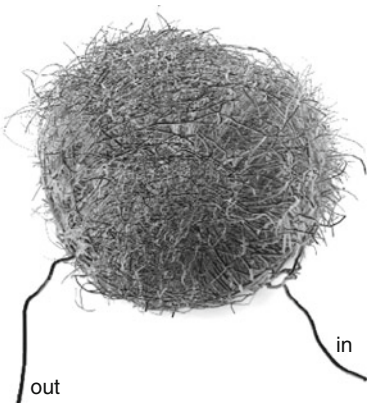

Fig. 4.7 Computational simulation of the vascular network in a tumor

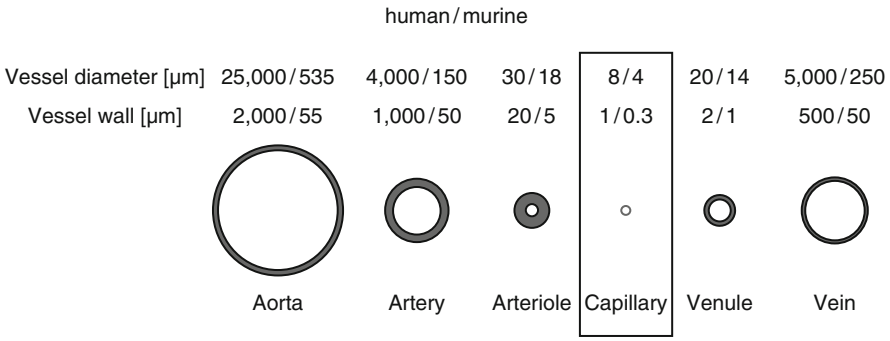

Fig. 4.8 Dimensions of blood vessels in humans resp. mice

to support the development of strategies against cancer, computer models were developed and related simulations performed [6]. Figure 4.7 shows such a model of the vascular network inside cancerous tissue.

However, for the validation of the theoretical network, a comparison between these models and the real blood vessel formation should be performed. Figure 4.8 shows typical dimensions of the different blood vessels of a human and for comparison of mice. In order to uncover even the smallest capillaries, an imaging technique with a spatial resolution down to the micrometer level is required. For such soft tissue, the density resolution of absorption contrast CT is not high enough for the differentiation of the blood vessels and the surrounded tissue. One possibility to enhance the contrast would be the staining of the blood vessels using a highly absorbing contrast agent [7–9]; another possibility would be phase contrast CT (see Sect. 4.2.4) which yields enough contrast even for aqueous specimens [8] where human derived mouse tumors were investigated.

In this section, we will deal with a third possibility to visualize the vascular network. Before the CT in absorption contrast of the tumor, a corrosion cast of

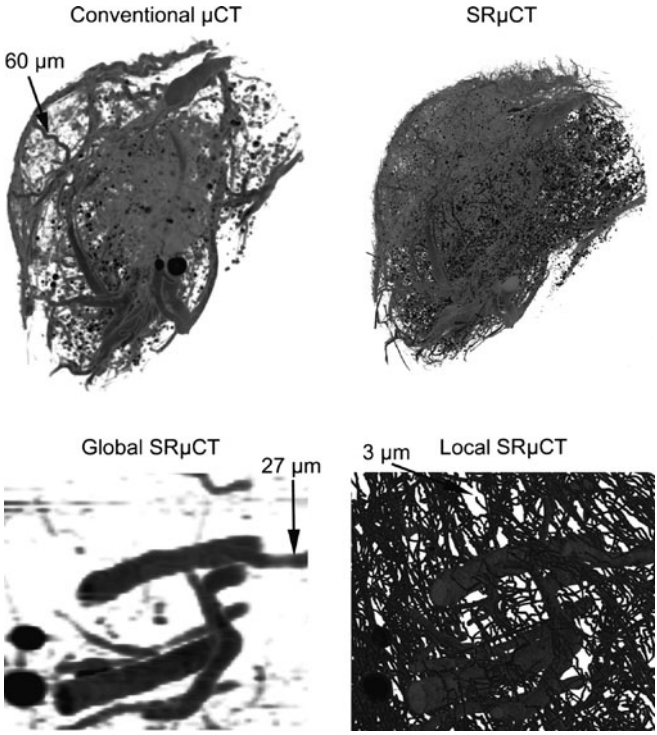

Fig. 4.9 SRμCT Three-dimensional representation of a cast of blood vessels inside a tumor acquired with conventional and synchrotron radiation-based microcomputed tomography in absorption contrast mode

the circulatory system of the mouse has to be fabricated [10]. In order to improve the contrast, the hardened polyurethane cast can be stained by OsO_4. The resulting three-dimensional renderings obtained by conventional CT and SRμCT can be seen in Figs. 4.9 and 4.14. First, the extracted tumor cast was scanned by means of the SkyScan 1174^{TM} system (SkyScan, Kontich, Belgium) at the selected acceleration voltage of 30 kV and the pixel size of 12 µm. The examination of this dataset showed that it is almost impossible to resolve blood vessels with diameters smaller than 50 µm. The SRμCT measurements were carried out at TOMCAT beamline at the Swiss Light Source [11] (Paul Scherrer Institute, Switzerland) with the selected energy of 15 keV. A total of 1,500 projections in equidistant angular steps of 0.12° between 0° and 180° were acquired. With the resulting detector pixel size induced by the first objective of 5.92 µm and the field of view of 12 mm, the whole specimen could be scanned (global tomography). However, these results only allowed to resolve vessel diameters larger than 20 µm. In order to visualize smaller capillaries, a second scan with another objective with a magnification of 10 and the resulting pixel size of 0.74 µm was arranged. These adjustments involved a field of view of

1.5 mm so that only a part of the specimen could be scanned (local tomography). Using this method, it was possible to resolve blood vessel diameters of around 3 μm.

4.2.3.2 Microstructure of Human Tooth

Human teeth are composed by two hard tissues, i.e. enamel and dentin. Enamel is the hard, brittle upper part of the tooth. It consists mainly of inorganic carbonated calcium phosphates with as little as 4% weight of organic material. Dentin is softer and tougher, and is composed of roughly 20 wt% of organic material, mainly collagen type I.

Teeth have rather limited reparation and regeneration capacities. While dentin can to some extent repair damages by formation of tertiary dentin, no self-repairing processes to counteract carious lesions or mechanically induced cracks or material loss is known in enamel. When the functionality of teeth is severely reduced by carious infection or mechanical action, it often becomes necessary to replace part of the damaged tissue or even the whole tooth with dental biomaterials or protheses.

Even though the quality of such replacements has constantly improved, their performance does not reach that of sound teeth, resulting in a limited lifespan that can render necessary further clinical interventions [12, 13]. It is, therefore, desirable to avoid the removal of tooth hard tissue whenever possible. Therefore, mechanisms that can restore the functionality of damaged teeth are matter of research. For example, induced repair mechanisms by means of bioactive glass have been proposed [14, 15]. A knowledge of the tooth microstructure will help to understand such processes as well as uncover to what extent the microarchitecture of teeth influences the formidable performance of human teeth.

Figure 4.10 shows three orthogonal slices through the three-dimensional tomographic dataset of a 700-μm-thin rod extracted from a human premolar, acquired at the TOMCAT beamline at the Swiss Light Source (Paul Scherrer Institute, Switzerland) [11], with a photon energy of 15 keV, exposure time of 170 ms, and isotropic pixel size of 0.37 μm. Dentin (dark gray) and enamel (light gray) can be clearly distinguished due to their different X-ray absorption. The circular arc on the right of the top left slice is an artifact caused by the fact that the tooth specimen was larger than the field of view.

In the dentin, tubular structures are visible as dark spots and streaks. These structures are known as dentinal tubules and serve the purpose of transportation of organic material and information between the pulp and the dentin. Diameter and density of the tubules vary over the specimen. Although the tubules are usually parallel, their orientation can change to become perpendicular to the dentin–enamel interface. Some of the tubules even spread across the interface and continue through the enamel.

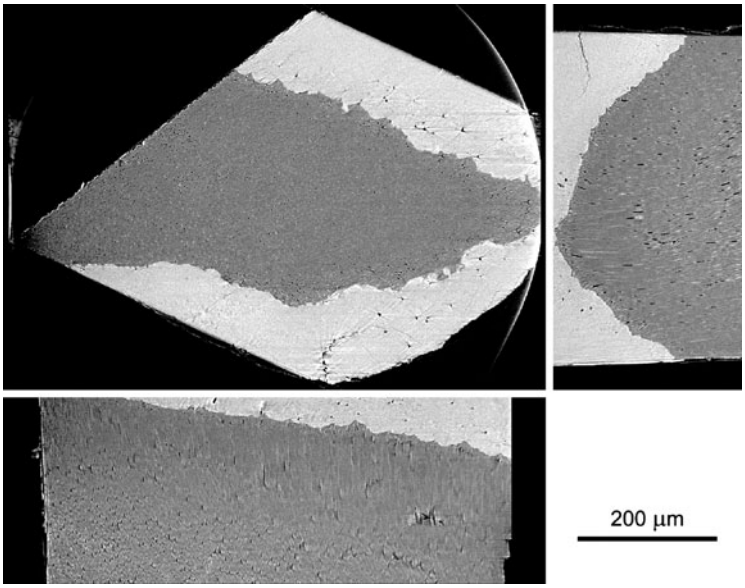

Fig. 4.10 Three orthogonal slices through a high resolution absorption contrast tomographic scan of a part of human tooth acquired at the TOMCAT beamline at the Swiss Light Source (Paul Scherrer Institute, Switzerland)

4.2.3.3 Imaging the Human Inner Ear

The morphology of the human hearing organ, which belongs to the most complex anatomical structures in the human body, is essential to achieve a better understanding of the inner ear pathologies (malformations) to improve the design and the insertion procedures of adapted cochlear implants as well as the treatment of hearing diseases.

Figure 4.11 shows a selected virtual cut of the sensory organ in the apical turn of the human cochlea and two schemes which should help identifying the morphological features. These SRμCT measurements were performed at the beamline BW2 (DESY, Germany) [16] at the selected photon energy of 10.8 keV, the resulting pixel size of 2.1 µm, and the spatial resolution of 4.3 µm characterized by the 10% value of the modulation transfer function (MTF) [17]. During the data acquisition, 720 projections over 180° were recorded. Before the SRμCT experiment, the specimen was osmium stained in order to increase the contrast of the tissue [18, 19]. The osmium stain served for the visualization of the Reissner membrane and permitted the thickness measurement with reasonable precision. It corresponds to two cell layers with a thickness of (10 ± 2) µm.

Another dataset even shows the visualization of individual ganglion cells [18] within the human tissue which can be seen in Fig. 4.12. The measurements were carried out at the TOMCAT beamline of the Swiss Light Source (Paul Scherrer

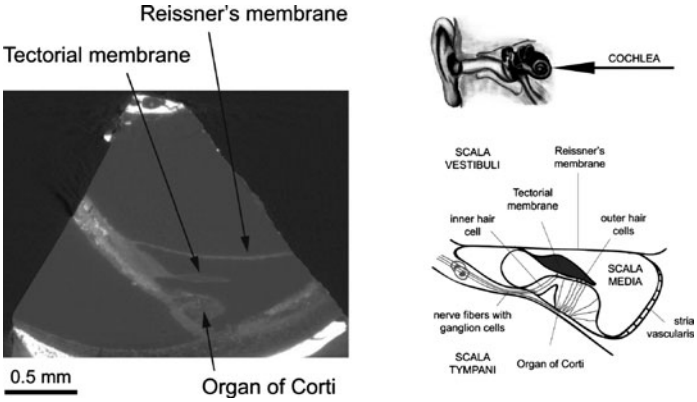

Fig. 4.11 Reconstructed slice of an absorption contrast SRμCT dataset (*left*) and a schematic representation (*right*) of a human inner ear

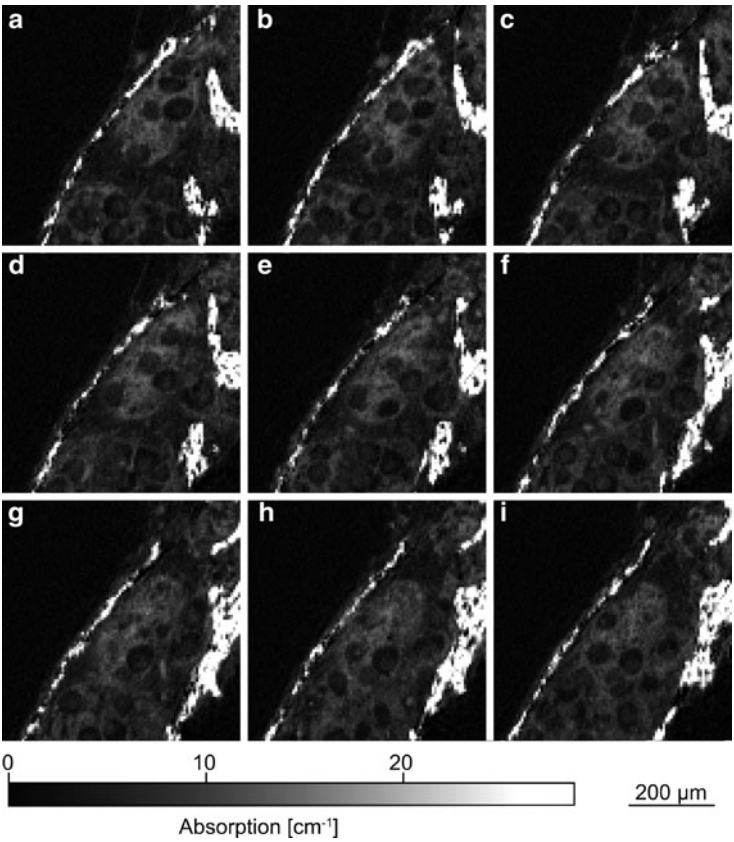

Fig. 4.12 Series of slices of absorption contrast SRμCT. Osmium-stained ganglion cells can be identified

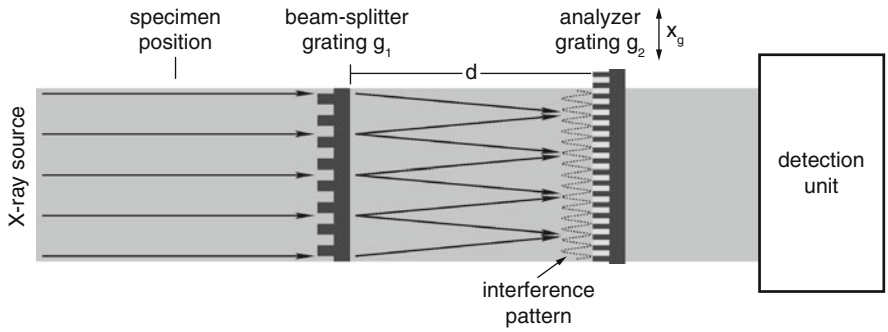

Fig. 4.13 Top view of the grating-based phase contrast setup

Institute, Switzerland) [11]. The data were acquired at the photon energy of 12 keV and an effective pixel size of 1.75 μm. A total of 1,501 projections between 0° and 180° were recorded. The neuron cell counting in a selected volume of 125 μm × 800 μm × 600 μm = 0.06 mm^3 gives rise to the estimate that 2,000 ganglion cells are present along 1 mm Organ of Corti.

4.2.4 Grating-Based X-Ray Phase Contrast CT

4.2.4.1 Instrumentation

Contrary to the absorption contrast, where the local X-ray absorption coefficient distribution $\mu(x, y, z)$ can be measured, phase-contrast CT provides the real part of the refractive index, often expressed in terms of its decrement from unity $\delta(x, y, z)$. This method is more advantageous than absorption contrast for specimens with small atomic numbers, particularly soft tissue. For X-ray energies far away from the absorption edges, it is related to the electron density distribution $\rho_e(x, y, z)$ via the equation

$$\delta(x, y, z) = \frac{r_e \lambda^2}{2\pi} \rho_e(x, y, z), \tag{4.3}$$

where r_e is the classical electron radius [20]. The detection of $\delta(x, y, z)$ can be achieved by a grating interferometer as schematically illustrated in Fig. 4.13, which is composed of a beamsplitter and an analyzer grating. The beam-splitter grating g_1 consists of silicon stripes with the periodicity p_1. It induces fringe patterns in the X-ray intensity distribution. At so-called Talbot distances from the beam-splitter grating of

$$d_n = \frac{n p_1^2}{8\lambda}, \tag{4.4}$$

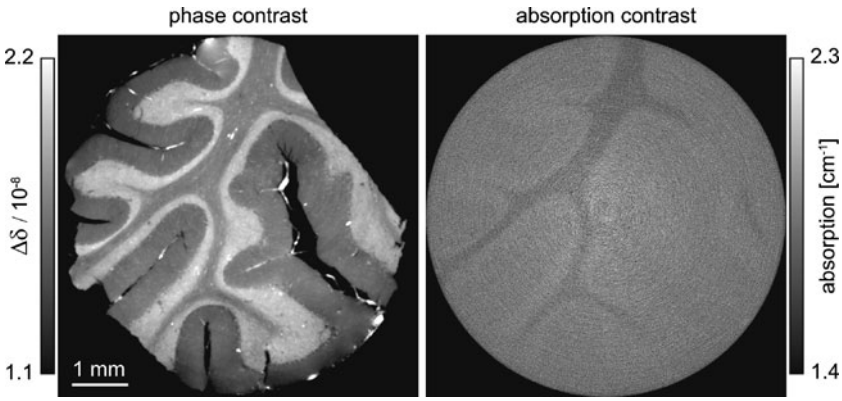

Fig. 4.14 Grating interferometry phase-contrast reconstruction of a human cerebellum acquired at the beamline ID19 (European Synchrotron Radiation Facility, France) plus the accordant slice obtained in absorption contrast mode at the beamline BW2 (HASYLAB at DESY, Germany)

the intensity fringe contrast takes extreme values at odd Talbot orders $n = 1, 3, 5, \ldots$, and vanishing contrast for even values of n [21]. For a phase contrast CT experiment, the distance between the grating g_1 and the analyzer grating g_2 equals the Talbot distances with odd Talbot orders. A phase object causes slight deflection of the incoming X-rays. The grating g_2 with a periodicity $p_2 = p_1/2$ has strongly absorbing stripes, here made of gold. This grating allows the detection of the disturbance of the interference pattern by using a phase stepping method where several images at different positions x_g of the grating g_2 are recorded [20]. The equation

$$\alpha(y,z) = \frac{\lambda}{2\pi}\frac{\partial\Phi(y,z)}{\partial y} = \int_{-\infty}^{\infty}\frac{\partial\delta(x,y,z)}{\partial y}\mathrm{d}x \tag{4.5}$$

describes the quantitative relation between the local beam propagation direction $\alpha(y,z)$, the wave phase shift $\Phi(y,z)$, and the decrement of X-ray refractive index $\delta(x,y,z)$.

4.2.4.2 Comparison Between Phase- and Absorption Contrast CT and Magnetic Resonance Microscopy

The power of phase contrast CT for aqueous specimens becomes apparent by comparing it with the other well-established techniques namely absorption contrast and magnetic resonance microscopy. Figure 4.14 shows one reconstructed slice of a human cerebellum piece in phase contrast and absorption contrast mode. The specimen was fixated in 4% formalin solution.

The grating-based phase contrast experiment was carried out at the beamline ID19 (European Synchrotron Radiation Facility, France) [22] with a selected photon energy of 23 keV using a double-crystal Si(111) monochromator in Bragg geometry.

The X-rays were taken from an undulator. The period of the beam-splitter grating was $p_1 = 4.785\,\mu\text{m}$ and of the analyzer grating $p_2 = 2.400\,\mu\text{m}$. As the experiment was carried out at the ninth Talbot distance, a distance of $d = 479.4\,\text{mm}$ between the gratings was adjusted. The Eppendorf container with the cerebellum in formalin solution was fixed at the high precision rotation stage and immersed in a water tank with parallel polymethylmethacrylat plates for the measurements in order to minimize artifacts owing to X-ray phase curvature induced by the container surface. For the detection, a lens-coupled scintillator and charge-coupled device (CCD) system using a FReLoN 2K (Fast-Readout, Low-Noise, ESRF Grenoble, France) CCD with 2,048 × 2,048 pixels with the effective pixel size of 5.1 μm was used. Four phase-stepping images were taken over one period of the interferometer fringe pattern at each projection angle. With an exposure time of 1 s for each image, 1,501 radiographs were recorded over a range of 360°. An estimation of the spatial resolution of the experimental data was obtained by means of Fourier analysis of the processed projections resulted in $(16.5 \pm 0.5)\mu\text{m}$ and of the reconstructed tomograms $(20 \pm 1)\mu\text{m}$.

The SRμCT experiments in absorption contrast mode were carried out at the beamline BW2 (HASYLAB at DESY, Germany) [16] using a monochromatic beam of 14 keV generated by a wiggler. Using a detector with a resulting pixel size of 3.0 μm 1,440 projections were acquired during the rotation of the specimen by 360°. The spatial resolution of the entire setup was determined by 10% of the MTF [17] corresponding to 6.48 μm. The projections were binned twofold before the reconstruction in order to improve the density resolution [23]. The twofold binning of the projected highly X-ray absorbing edge led to a reduced spatial resolution of 8.77 mm again determined by 10% of the MTF.

Whereas the reconstructed absorption contrast slice only shows marginal contrast between white (dark region) and gray matter (bright region), the phase contrast also allows, besides a clear differentiation between white and gray matter, a distinction within the gray tissue in the stratum moleculare (dark region of the gray mater) and the stratum granulosum (bright region of the gray matter).

For the visualization of human brain tissue or generally soft tissue, magnetic resonance tomography is a widely used technique. Today, it is irreplaceable in medicine because it delivers superb contrast between white and gray matter and it has no radiation damages for the patients. Therefore, a comparison between grating-based phase contrast and magnetic resonance tomography with better spatial resolution than the conventional medical scanners was done. The results acquired by high field magnetic resonance microscopy (Fig. 4.15) with a voxel size of 100 μm show a better contrast between the white and gray matter compared to the absorption contrast CT but the contrast is not good enough to differentiate between the two strata of the gray matter.

The three-dimensional rendering of the grating interferometry results clarifies the power of this technique. Figure 4.16 shows an intensity-based segmentation of the stratum granulosum. Besides the stratum granulosum, many blood vessels can be resolved without the use of any contrast agent. The most important finding of this dataset is that the high spatial resolution and the high sensitivity of this

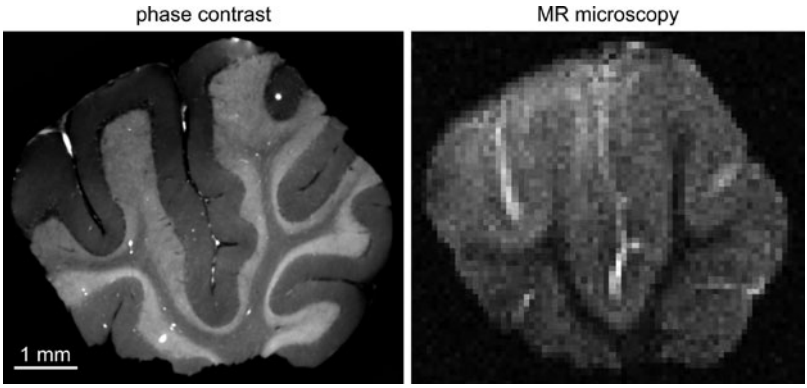

Fig. 4.15 Slice from the dataset of Fig. 4.14 and the accordant magnetic resonance microscopy image recorded at the Technische Universität München, Germany

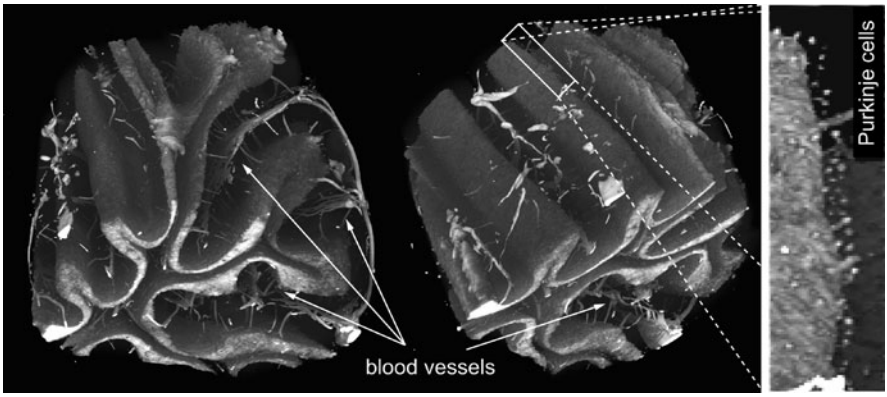

Fig. 4.16 Phase-contrast three-dimensional rendering of the human cerebellum block (cp. Fig. 4.14 *left*) showing various blood vessels and even individual Purkinje cells

imaging technique allows the detection of individual nonstained cells surrounded by soft tissue. The detection of individual Purkinje cells with spherical diameters of 40–70 μm without the application of any stain or contrast agent is a novelty in the field of computerized tomography [24].

4.2.4.3 Morphology of Human Urethra

Another application of the grating-based phase contrast is the morphological characterization of human urethra. As the number of incontinent patients is steadily increasing, the function of the urethra under static and, more important, under stress conditions has to be uncovered.

Figure 4.17 shows orthogonal cuts through a human urethra acquired by grating interferometry and clarifies the nonperfect symmetry along the opening.

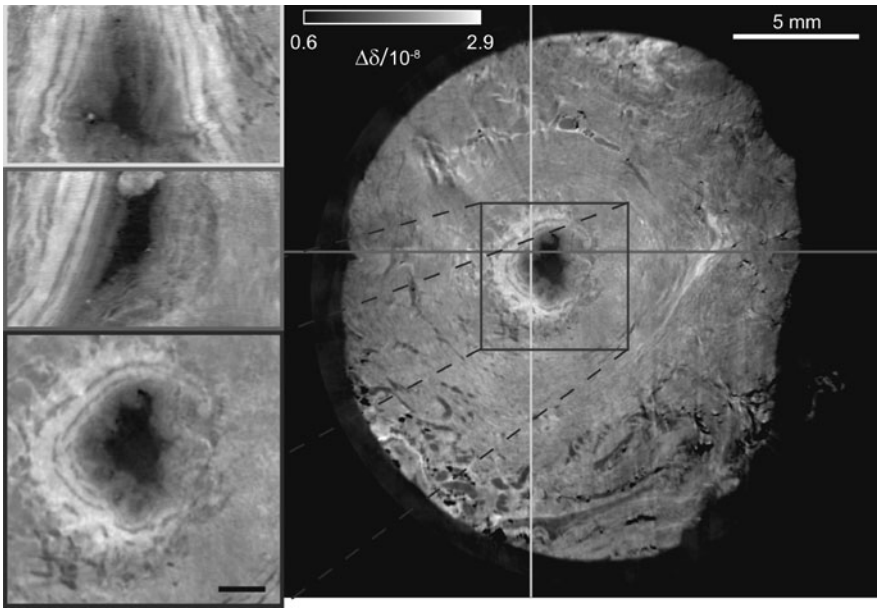

Fig. 4.17 Virtual cuts though a grating-based tomography data set of a human urethra acquired at the W2 beamline (DESY, Germany)

The measurements were performed at the beamline W2 (HASYLAB at DESY, Germany) with the recently established grating interferometer setup [25]. At the selected energy of 24 keV and a resulting pixel size of 10 μm and a spatial resolution of 37 μm 1,101 projections over 360° were recorded. The spatial resolution of the experimental setup was determined by the 10% of the MTF of a processed projection of a silicon wedge.

More information on the experimental details are given elsewhere [26]. The motivation of this study can be found in the recent message [27].

4.2.5 Small-Angle X-Ray Scattering

4.2.5.1 Instrumentation

Small-angle X-ray scattering (SAXS) belongs to the reciprocal space imaging techniques. It is characterized by a reciprocity law, which gives an inverse relationship between the size of the inspected particles and scattering angle. It occurs when an inspected specimen presents electron density inhomogeneities on the nanometer scale, thus resulting in scattering angles in the range of few mrad. SAXS is, therefore, of particular interest in fields where inhomogeneities at such length scales

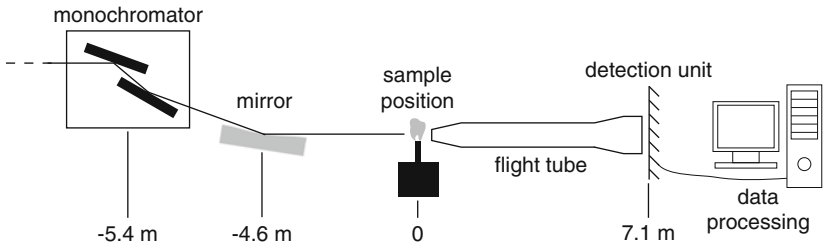

Fig. 4.18 Schematic representation of the cSAXS end-station

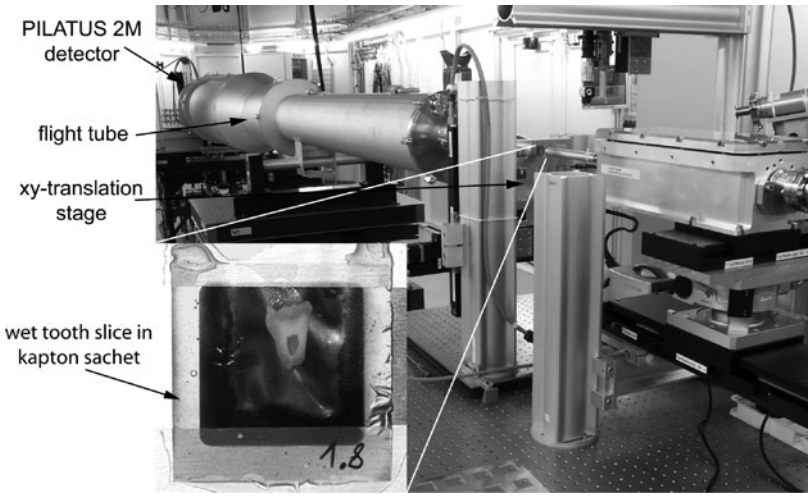

Fig. 4.19 The end-station at the cSAXS beamline at the Swiss Light Source (Paul Scherrer Institute, Switzerland)

occur, e.g., for the characterization of polymers [28], protein structures [29], or inspection of human tissues, e.g., cancerous and noncancerous tissue [30,44] myelin sheaths of neurons [31], dentin [32,33], or bone and cartilage [34,35].

In this section, a typical SAXS instrumentation on the example of the cSAXS beamline at the Swiss Light Source (Paul Scherrer Institute, Switzerland) [36] is given. Figure 4.18 gives a schematic representation of the endstation at the cSAXS beamline. Coming from the left, the X-rays pass through a fixed exit Si(111) monochromator, which allows to choose energies in the range between 4 and 19 keV. The second mirror crystal can be bent to allow for horizontal focussing of the X-ray beam, while a quartz glass mirror at 4.5 m from the sample allows for vertical focussing. The beam is normally focussed at the sample position to a spot size of approximately $5 \times 20\,\mu m^2$ (vertical $\times$ horizontal). A 7-m-long evacuated flight tube is placed between the sample and the PILATUS 2M detector [37] to minimize noise from air scattering. Dedicated data processing hardware and software is required for data evaluation. Figure 4.19 shows a photograph of the cSAXS endstation.

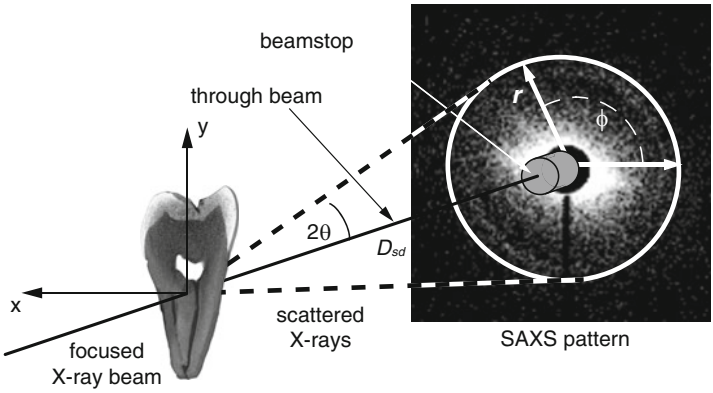

Fig. 4.20 Scanning SAXS data acquisition

Figure 4.20 depicts a typical experimental setup. The X-ray beam hits the sample perpendicularly. Only a fraction of the photons is scattered at the sample position, while the large part is transmitted through the sample. A sufficiently thin specimen is required to avoid excessive X-ray absorption in order to obtain sufficient photon statistics for data evaluation.

With the high-brilliance source combined with the fast detector technology available at cSAXS, imaging rates of up to 30 Hz are possible. These fast acquisition times allow to scan the sample through the beam in x and y directions while continuously recording images. In this setup, samples with areas in the cm^2 range can be scanned within 1 h or even less. The exact total acquisition time for the scanning X-ray scattering measurements depends on the number of spots in the raster scan and the exposure time used. The latter in turn will depend on the signal-to-noise ratio of the data, the X-ray absorption, and the scattering contrast in the sample.

To process the high amount of information generated, automated analysis routines are needed. The first step in SAXS data analysis consists in a radial integration of the scattering patterns over 16 radial segments in a specific q-range interval (Fig. 4.21, on the right). The intensity in each circular segment is then plotted as a function of its angular position θ (Fig. 4.21 left). If the scattering pattern presents a moderate asymmetric intensity distribution, the plot is well approximated by a cosine curve. The mean scattered intensity, indicated in Fig. 4.21 with I_{sym} relates to the abundance of scattering centers in the selected q-range, while the amplitude of the cosine I_{asym} relates to their orientation. The phase ϕ yields the mean orientation of the scattering signal.

As fitting, however, is time consuming and the results can significantly vary depending on the initial conditions and the goodness of the data, instead of a cosine-fit, the data are approximated with a Fourier transform

$$I(\theta) \cong I_{\text{sym}} + I_{\text{asym}} \cdot \cos(\theta + \phi). \tag{4.6}$$

For specimens with strong orientation on the nanometer scale however, the intensity distribution can differ from an ideal cosine assumed by the Fourier analysis. The

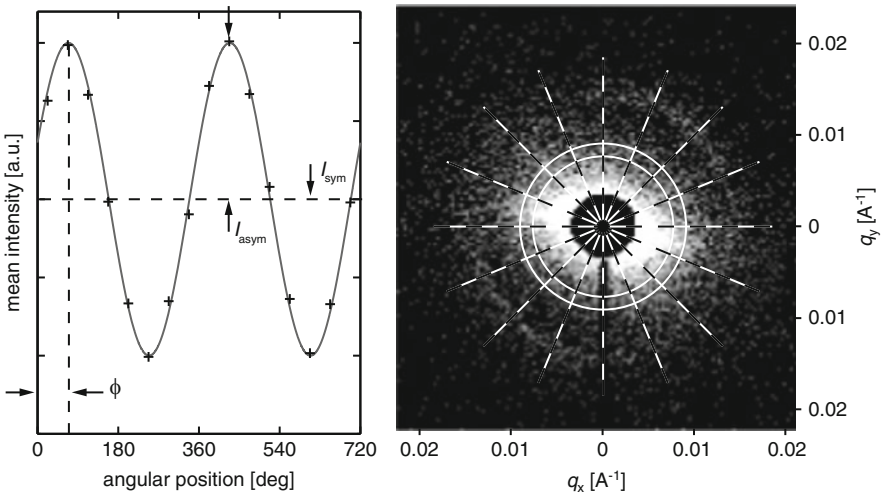

Fig. 4.21 Processing of a SAXS pattern

deviation from the cosine is expected to be significant in strongly oriented areas and indicates that for highly ordered materials, different analysis schemes could be worth trying.

Additional information can be extracted from the scattering patterns and from the radially integrated intensity. The exponent of the intensity curve $I(q)$ contains information about the geometrical shape of the scattering centers in the sample. Spherical scatterers will exhibit a q^{-4} intensity fall off, whereas flat lamellar or disc-like structures will have an exponent closer to -2 and elongated, rod-, or needle-like features an exponent of -1. As the scattering patterns possess an inversion symmetry around the beam center, one can look at asymmetries of the scattered intensity with respect to this inversion center. This signal contains information similar to that obtained by grating interferometry (cp. Sect. 4.2.4.1). Like it is the case for a true grating interferometry signal, topographical features like edges and scratches become clearly visible.

4.2.5.2 Nanostructures of the Human Tooth

Human tooth hard tissues present strong preferential orientations on the nanometer scale. Figure 4.22 shows a collection of SAXS data of a 400-μm-thin slice extracted from human third molar in the q-range between 0.021 and 0.016 Å^{-1}, corresponding to the range between 30 and 40 nm in real space, acquired at the cSAXS beamline [36] at 18.58 keV photon energy with 180 ms exposure time per frame and a step size between the raster scan points of 50 μm in both x and y directions.

The symmetric intensity (top-left image), related to the density of scatterers in this range, shows a strong increase near the dentin–enamel junction (DEJ), indicating a high abundance of nanostructures. The orientation of the scattering

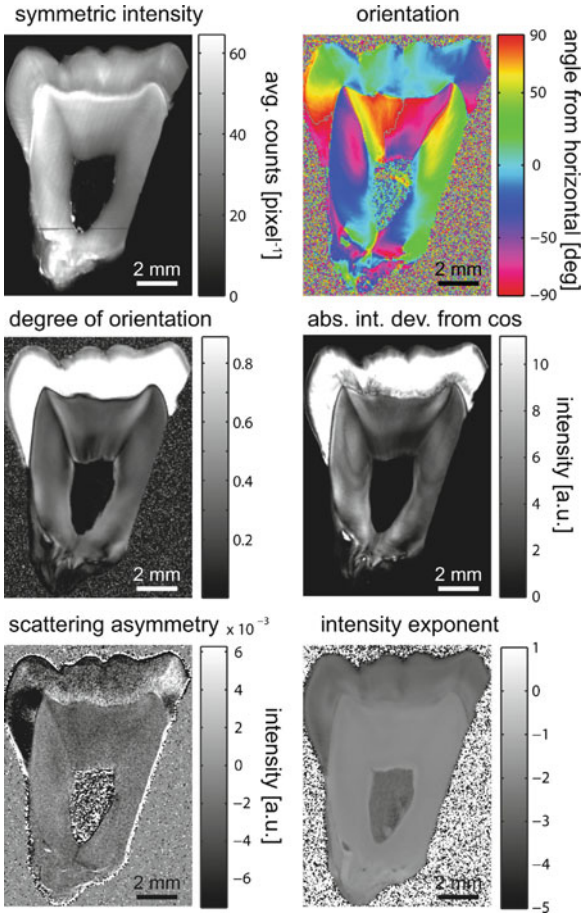

Fig. 4.22 Different information routinely extracted from scanning SAXS data at the cSAXS beamline illustrated on the basis of a human tooth slice

signal (top-right image), which is perpendicular to the orientation of the scattering nanostructures, shows clear differences between enamel and dentin. While the signal is mostly oriented parallel to the DEJ through the whole of the enamel, it is mainly oriented parallel to the DEJ in the upper part of the dentin. Sharp changes in dentin orientation can be observed at lines connecting the tooth cusps and the pulp. The degree of orientation (middle left image), defined as the ratio of oriented to unoriented scattered intensity $I_{\mathrm{sym}}/I_{\mathrm{asym}}$, relates to the degree of anisotropy in the plane perpendicular to the incident X-ray beams. Much higher directional organization is found in the enamel, while the degree of orientation in the dentin slightly decreases from the DEJ toward the pulp. As expected, the deviation of the integrated intensity from an ideal cosine (middle right image) strongly resembles the orientation pattern, with high values in the strongly oriented enamel and reduced intensity in the dentin. The scattering asymmetry signal (bottom left image) yields a rather homogeneous signal in both enamel and dentin, with strong shifts at the edges of the specimen, indicating the absence of sharp edges or cracks inside the

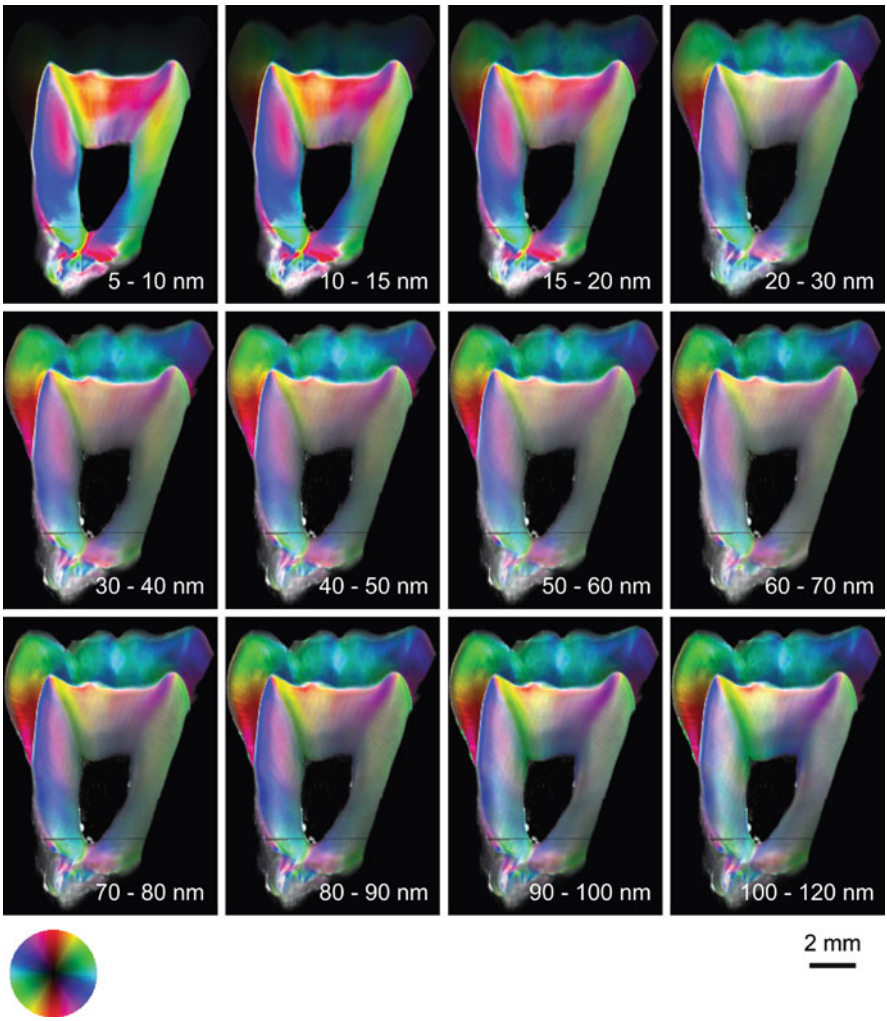

Fig. 4.23 Orientation, abundance, and degree of orientation of different sizes of nanostructures of a human tooth slice (cp. Fig. 4.22). The main orientation of the scattering signal is color-coded (see color wheel). The color intensity codes the scattered intensity, while the color saturation codes the degree of orientation of the scattering signal

tooth slice. The intensity exponent, related to the shape of the scatterers, is given in the bottom right image. In the investigated range, the dentin contains more needle- or rod-like scatterers, thus giving raise to an intensity decay proportional to q^{-1}, whereas the signal in the enamel indicates the presence of two-dimensional scatterers with an intensity profile proportional to q^{-2}.

Figure 4.23 shows the combined information of total scattered intensity I_{sym}, orientation ϕ and degree of orientation $I_{\mathrm{asym}}/I_{\mathrm{sym}}$ for different q-ranges of the same

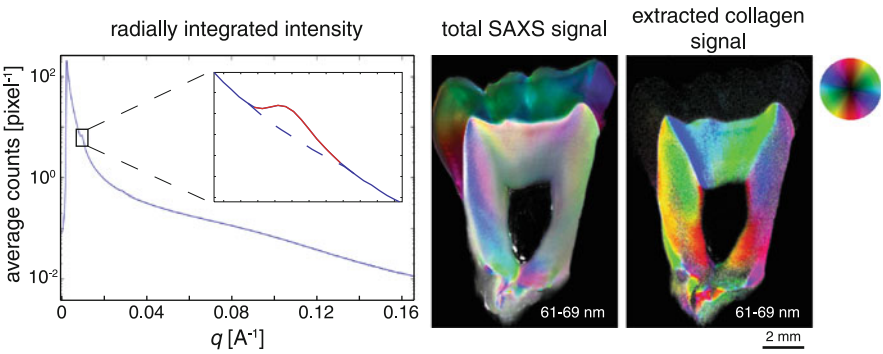

Fig. 4.24 Radially integrated intensity of a typical SAXS pattern of dentin exhibiting a characteristic peak related to collagen. The collagen signal can be extracted and processed separately

tooth slice. The orientation of the scattering material is according to the color wheel, showing which color represents which orientation. Bright colors mean more total scattering intensity than dim colors. Effectively oriented material shows up in color whereas unoriented material shows up white. Gray shades mean less unoriented material than in white areas.

The scattering signal in the enamel disappears below 10 nm, indicating that the smallest extension of the nanocrystallites composing the enamel lies above 10 nm [38]. For all length scales, the main orientation in enamel and dentin is comparable, with the scattering signal parallel to the DEJ in the enamel and perpendicular in the dentin. However, the degree of orientation diminishes toward larger length ranges, and higher anisotropies are found toward the enamel compared to the region surrounding the pulp. Abrupt changes in dentin orientation can be seen along lines connecting the tooth cusps and the pulp over all ranges. The changes are sharper toward low and high ranges, while they are blurred out between 30 and 70 nm.

Dentin is composed to 20 wt% of organic material, mainly collagen-I fibrils [39]. The building blocks of collagen arrange themselves along the collagen fibril with a main periodicity of 67 nm, as determined, for example, by means of atomic force microscopy and SAXS [40]. This periodicity gives rise to a distinct peak in scattered intensity at the corresponding q range between about 0.009 and 0.01 Å^{-1}. Due to the disposition of the building blocks inside the collagen fibrils, this peak-like scattering signal is parallel to the collagen fibrils.

The plot in Fig. 4.24 shows a typical intensity profile $I(q)$ of dentin after radial integration and a magnification of the region containing the collagen peak. The background intensity below the peak can be fitted with a power-law exponent close to -2. After subtracting the background from the total signal, the remaining intensity is solely associated to the scattering signal from the collagen. The two images in Fig. 4.24 show the orientation, degree of orientation, and total scattering intensity both before and after background subtraction for the range between 61 and 69 nm. As expected, no significant signal can be seen in the enamel after the

background subtraction, due to its anorganic nature. The scattering signal associated with the collagen shows a perpendicular orientation to the total scattering signal in the dentin, indicating that collagen fibrils are oriented parallel to the dentin crystallites, which make up for the largest part of the total SAXS signal.

4.3 Conclusion

Since the discovery in 1895 by Röntgen [2], X-rays have played a dominant role in our everyday life. For example, they make the bones in our body visible, serve for the nondestructive testing of a wide variety of materials including human tissues postmortem, and enhance our security in air travel.

Some time later, M. von Laue and others discovered and interpreted X-ray diffraction in crystals [41], which provided a wealth of information about solid states including the arrangement of atoms.

X-ray spectroscopy techniques made it possible to nondestructively determine the chemical composition of solids simply by analyzing the X-ray fluorescent spectra when the atoms were excited. With a focused X-ray source realized at different synchrotron radiation facilities, one can not only determine the chemical composition with reasonable spatial resolution but also get access to nanostructures in the entire nanometer range.

Today, highly intense X-ray sources as the free electron lasers allow measurements within such a small time interval that the molecule of interest does not have enough time to become destroyed.

In medicine, X-ray imaging attracted the greatest interest, since the penetrating power of X-rays reveals the bulk properties of the body rather than the surface shape. We mainly see the bones because of the strong dependence of attenuation on the atomic number. The limitation in spatial resolution is mainly given by the detection unit and not by the X-ray source or the stability of manipulator for rotation. The availability of powerful computing resources has permitted the tomographic reconstruction of the three-dimensional microstructure of the specimen or the entire human body. High spatial resolution, however, requires a related photon density and dose, so that a spatial resolution below 50 μm cannot be reached for in vivo studies.

Synchrotron radiation facilities have a restricted availability and therefore require a different working regime. The scientists have to carefully prepare their experiments, much more carefully than in a conventional laboratory. They have to organize their work during the 24 h per day experiment in an efficient manner and have finally plenty of time for the data treatment and the publication of the results. The main advantage of the synchrotron radiation sources, however, is their intensity and brightness, which are numerous orders of magnitudes higher than conventional bremsstrahlung sources. It allows incorporating a monochromator and still having a sufficiently high intensity for the experiment to be performed in reasonable time frames.

The microstructures within the human tissues can be made visible postmortem by means of SRμCT. These microstructures include the vessel tree of healthy and cancerous tissues, which enable a direct comparison also with simulations to validate them. Gathering the smallest capillaries is here of upmost interest, because the vascularization of tumors is often much better, although they can also contain a necrotic core. Dentinal tubules play a major role in the supply of the dentin. Their density and orientation reflect the history of the tooth. The complete characterization of the dentin's morphology is a vital step toward the quantitative understanding on why restorations can fail even if the clinical procedures are maintained constant. Only a very few research teams worldwide have been able to uncover the tubules using hard X-ray tomography [33, 42].

It is a dream of the researchers to build a human out of individual cells. Hence, the visualization of the individual cells within the human body is an interesting challenge. The membranes of the inner ear (double layer of cells) belong to the first structures, which were imaged in its three-dimensional shape. This is very important, as in histological sections the membranes relax and usually appear as straight line. The human cochlea, however, has two and a half turns so that the membranes have to exhibit a curved shape. The first example of identification of individual cells in humans by hard X-ray tomography is the successful visualization of hundreds of ganglion cells of the inner ear, which were osmium stained. Very recently, using the grating-based phase contrast tomography, even unstained Purkinje cells came to light. It will take another decade until about hundred cell types within the human body can be imaged with the necessary resolution. Here, the phase contrast will play a more and more important role, since the contrast especially is orders of magnitudes better than in the conventional absorption contrast.

Scanning SAXS uncovers a wealth of information on the nanostructures in human tissues over macroscopic areas in real space. The identification of the specific features from the scattering patterns needs additional information, which requires detailed medical knowledge. So far data of human tissues are available from healthy and carious teeth, bone and cartilage, healthy and malign breast biopsies, as well as male and female urethras. In all cases, one finds a high degree of organization along the entire nanometer range for both hard and soft tissues in humans. Human tissues exhibits a strong anisotropy often related to the direction of mechanical loading.

We do expect that scanning SAXS will play a dominant role in the further development of nanomedicine and related fields. One example, namely bioinspired dental fillings that should have different orientations on the nanometer scale within the dentin and the enamel has been already published and will help to further understand the unique mechanical properties of our denture. The actual realization of the nanoscopic anisotropy of the fillings, however, is still a challenge for the researchers in the field of nanodentistry.

Acknowledgements The authors are grateful for the support of numerous researchers. In particular, the experimental support and the support in the SAXS data treatment of O. Bunk (Paul Scherrer Institut, Villigen, Switzerland), the valuable assistance in SRμCT by F. Beckmann and

J. Herzen (HZG, Hamburg, Germany), the experimental support and help in image generation of tumors by S. Lang (BMC, Basel Switzerland), the provision of the simulation data of the tumor by D. Szczerba (ETH Zrich, Switzerland), and the support of A. Lareida (BMC, Basel Switzerland) preparing the tomography data and the scheme on the inner ear are gratefully acknowledged.

The beamtimes were granted on the basis of the following approved beamtime applications: "Microcomputed tomography of human brain tissue using grating-based phase contrast" (MD-328, ESRF Grenoble France), "Microcomputed tomography of human brain for the nonrigid registration of histological slices" (II-20060035 EC, HASYLAB at DESY Hamburg Germany), "Remineralization studies of dentin by microcomputed tomography," and "Three-dimensional high-resolution imaging the cellular structure of the human inner ear" (SLS at PSI, Villigen Switzerland).

References

1. J. Als-Nielsen, G. Materlik, Phys. Today **48** (11), 34 (1995)
2. W.C. Röntgen, Ann. Phys. **64**, 1 (1898)
3. A.C. Kak, M. Slaney (ed.), *Computerized Tomographic Imaging* (IEEE Press, New York, 1988)
4. E. Jöhnsson, Dissertation, University of Uppsala (1928)
5. L. Grodzins, Nucl. Instrum. Methods **206**, 541 (1983)
6. B.A. Lloyd, D. Szczerba, M. Rudin, G. Székely, Philos. Trans. R. Soc. London, Ser. A **366** (1879), 3301 (2008)
7. S. Lang, M. Dominietto, B. Müller, in *Journal of Physics: Conference Series 186*, Zurich, 2009, ed. by C. Quitmann, C. David, F. Nolting, F. Pfeiffer and M. Stampanoni
8. B. Müller, S. Lang, M. Dominietto, M. Rudin, G. Schulz, H. Deyhle, M. Germann, F. Pfeiffer, C. David, T. Weitkamp, in *Proceedings of SPIE 7078*, San Diego, 2008, ed. by S.R. Stock
9. B. Müller, J. Fischer, U. Dietz, P. Thurner, F. Beckmann, Nucl. Instrum. Methods Phys. Res., Sect. B **246**, 254 (2006)
10. T. Krucker, A. Lang and E.P. Meyer, Microsc. Res. Tech. **69** (2), 138 (2006)
11. M. Stampanoni, A. Groso, G. Isenegger, G. Mikuljan, Q. Chen, A. Bertrand, S. Henein, R. Betemps, U. Frommherz, P. Boher, D. Meister, M. Lange, R. Abela, in *Proceedings of SPIE 6318*, San Diego, 2006, ed. by U. Bonse
12. K. Sunnegardh-Grönberg, J.W.V. VanDijken, U. Funegard, J. Dent. **37**, 673 (2009)
13. J.-P. VanNieuwenhuysen, W. D'Hoore, J. Carvalho, V. Qvist, J. Dent. **31**, 395 (2003)
14. T. Waltimo, T.J. Brunner, M. Vollenweider, W.J. Stark, M. Zehnder, J. Dent. Res. **86** (8), 754 (2007)
15. F. Kernen, T. Waltimo, H. Deyhle, F. Beckmann, W. Stark, B. Müller, in *Proceedings of SPIE 7078*, San Diego, 2008, ed. by S. Stock
16. F. Beckmann, J. Herzen, A. Haibel, B. Müller, A. Schreyer, in *Proceedings of SPIE 7078*, San Diego, 2008, ed. by S. Stock
17. B. Müller, P. Thurner, F. Beckmann, T. Weitkamp, C. Rau, R. Bernhardt, E. Karamuk, L. Eckert, S. Buchloh, E. Wintermantel, D. Scharnweber, H. Worch, in *Proceedings of SPIE 4503*, San Diego, 2002, ed. by U. Bonse
18. A. Lareida, F. Beckmann, A. Schrott-Fischer, R. Glueckert, W. Freysinger, B. Müller, J. Microsc. **234**, 95 (2009)
19. B. Müller, A. Lareida, F. Beckmann, G.M. Diakov, F. Kral, F. Schwarm, R. Stoffner, A.R. Gunkel, R. Glueckert, A. Schrott-Fischer, J. Fischer, A. Andronache, W. Freysinger, in *Proceedings of SPIE 6318*, San Diego, 2006, ed. by U. Bonse
20. T. Weitkamp, A. Diaz, C. David, F. Pfeiffer, M. Stampanoni, P. Cloetens, E. Ziegler, Opt. Expr. **13**, 6296 (2005)
21. T. Weitkamp, C. David, C. Kottler, O. Bunk, F. Pfeiffer, in *Proceedings of SPIE 6318*, San Diego, 2006, ed. by U. Bonse

22. T. Weitkamp, P. Tafforeau, E. Boller, P. Cloetens, J.-P. Valade, P. Bernard, F. Peyrin, W. Ludwig, L. Helfen, J. Baruchel, AIP Conf. Proc. **1221**, 33 (2010)
23. P. Thurner, F. Beckmann, B. Müller, Nucl. Instrum. Methods Phys. Res., Sect. B **225**, 599 (2004)
24. G. Schulz, T. Weitkamp, I. Zanette, F. Pfeiffer, F. Beckmann, C. David, S. Rutishauser, E. Reznikova, B. Müller, J. R. Soc. Interface **7**, 1665 (2010)
25. J. Herzen, F. Beckmann, T. Donath, M. Ogurreck, C. David, F. Pfeiffer, J. Mohr, E. Reznikova, S. Riekehr, A. Haibel, G. Schulz, B. Müller, A. Schreyer, in *Proceedings of SPIE 7804*, San Diego, 2010, ed. by S.R. Stock
26. B. Müller, G. Schulz, J. Herzen, S. Mushkolaj, T. Bormann, F. Beckmann, K. Pschel, in *Proceedings of SPIE 7804*, San Diego, 2010, ed. by S.R. Stock
27. B. Müller, SPIE Newsroom (2010) DOI 10.1117/2.1201009.003123
28. H.S. Mansur, R.L. Oréfice, A.A.P. Mansur, Polymer **45**, 7194 (2004)
29. J. Lipfert, L. Columbus, V. B. Chuc, S. Doniach, J. Appl. Crystallogr. **40**, 235 (2007)
30. G. Falzon, S. Pearson, R. Murison, C. Hall, K. Siu, A. Evans, K. Rogers, R. Lewis, Phys. Med. Biol. **51**, 2465 (2006)
31. M. De Felici, R. Felici, C. Ferrero, A. Tartari, M. Gambaccini, S. Finet, Phys. Med. Biol. **53**, 5675 (2008)
32. J.H. Kinney, J.A. Pople, G.W. Marshall, S.J. Marshall, Calcif. Tissue Int. **69**, 31 (2001)
33. H. Deyhle, O. Bunk, S. Buser, G. Krastl, N. Zitzmann, B. Ilgenstein, F. Beckmann, F. Pfeiffer, R. Weiger, B. Müller *Proceedings of SPIE 7401*, San Diego, 2009 ed. by R.J. Martn-Palma and A. Lakhtakia
34. O. Paris, I. Žizăk, H. Lichtenegger, P. Roschger, K. Klaushofer, P. Fratzl Cell. Mol. Biol. **46**, 993 (2000)
35. A. Cedola, M. Mastrogiacomo, S. Lagomarsino, R. Cancedda, C. Giannini, A. Guagliardi, M. Ladisa, M. Burghammer, F. Rustichelli, V. Komlev, Spectrochim. Acta B. **62**, 642 (2007)
36. O. Bunk, M. Bech, T.H. Jensen, R. Feidenhansl, T. Binderup, A. Menzel, F. Pfeiffer, New J. Phys. **11**, 123016 (2009)
37. P. Kraft, A. Bergamaschi, C. Broennimann, R. Dinapoli, E.F. Eikenberry, B. Henrich, I. Johnson, A. Mozzanica, C.M. Schlepütz, P.R. Willmott, B. Schmitt, J. Synchrotron. Radiat. **16**, 368 (2009)
38. A. Vieira, R. Hancock, H. Limeback, M. Schwartz, M. Grynpas, J. Dent. Res. **82**, 909 (2003)
39. M.V. Stack, Ann. NY. Acad. Sci. **60**, 585 (1955)
40. M. Balooch, S. Habelitz, J.H. Kinney, S.J. Marshall, G.W. Marshall, J. Struct. Biol. **162**, 404 (2008)
41. W. Friedrich, P. Knipping, M. Laue, Ann. d. Phys. 346, 971 (1913)
42. S.R. Stock, A.E. Vieira, A.C. Delbem, M.L. Cannon, X. Xiao, F.D. Carlo, J. Struct. Biol. 161, 144 (2008)
43. J. Radon, Ber. Verh. Konigl. Sachs. Ges. Wiss. **69**, 262 (1917)
44. B. Müller, H. Deyhle, D. Bradley, M. Farquharson, G. Schulz, M. Müller-Gerbl, O. Bunk, Eur. J. Nanomed. **3**, 30 (2010)